Biomechanics and Modeling in Mechanobiology
https://doi.org/10.1007/s10237-020-01394-5

ORIGINAL PAPER

A reduced-order model of the spine to study pediatric scoliosis

Sunder Neelakantan[1] · **Prashant K. Purohit**[1] · **Saba Pasha**[2]

Received: 30 March 2020 / Accepted: 30 September 2020

Abstract
The S-shaped curvature of the spine has been hypothesized as the underlying mechanical cause of adolescent idiopathic scoliosis. In earlier work, we proposed a reduced-order model in which the spine was viewed as an S-shaped elastic rod under torsion and bending. Here, we simulate the deformation of S-shaped rods of a wide range of curvatures and inflection points under a fixed mechanical loading. Our analysis determines three distinct axial projection patterns of these S-shaped rods: two loop (in opposite directions) patterns and one Lemniscate pattern. We further identify the curve characteristics associated with each deformation pattern, showing that for rods deforming in a Loop1 shape the position of the inflection point is the highest and the curvature of the rod is smaller compared to the other two types. For rods deforming in the Loop2 shape, the position of the inflection point is the lowest (closer to the fixed base) and the curvatures are higher than the other two types. These patterns matched the common clinically observed scoliotic curves—Lenke 1 and Lenke 5. Our S-shaped elastic rod model generates deformations that are similar to those of a pediatric spine with the same sagittal curvature characteristics and it can differentiate between the clinically observed deformation patterns.

Keywords Spine · Scoliosis · Sagittal profile · Classification · Rod mechanics

1 Introduction

During the fast growth period around puberty, some pediatric spines deform in three dimensions leading to scoliosis (Burwell 2003; Castelein et al. 2005; Castelein and Veraart 1992; Weinstein et al. 2008). While the pathogenesis of this disease remains unknown (Gu et al. 2009; Liu et al. 2012), the side view of the S-shaped curvature of the fast-growing, flexible, immature, slender spines has been hypothesized as an underlying mechanical cause of adolescent scoliosis which also may impact the clinical management of the disease (Cheng et al. 2015; Pasha 2019a, b; Pasha and Baldwin 2019a; Schlösser et al. 2014). It has been clinically shown that at an early stage of scoliosis, the sagittal curvature of the spine is different between scoliotic and non-scoliotic subjects of similar age and sex (Schlösser et al. 2015). However, as the scoliosis changes the spinal alignment in three dimensions (Pasha et al. 2014a), even at an early stage of the disease (Brink et al. 2018), it is challenging to evaluate the role of the true sagittal alignment of the spine in induction of scoliosis. As the idiopathic scoliotic patients are otherwise healthy, identifying these patients before the onset of scoliosis in order to obtain their patterns of sagittal profile is difficult (Castelein and Veraart 1992).

We turn to simulations to test the hypothesis that changes in the S-shaped curvature of a rod, similar to the sagittal curvature of the spine, result in deformity patterns that are similar to the spinal deformity patterns in scoliosis. Previously, buckling of 2D rods was used to explain different deformation patterns in scoliotic spine (Belytschko et al. 1973; Lucas 1970). These deformations were explained based on the Euler's critical load that causes instability in a 2D rod model, and then, the buckling modes were compared to patterns of the spinal deformity in thoracic and lumbar spine (Crisco and Panjabi 1992; Crisco et al. 1992; Goto et al. 2003; Lucas and Boris 1961; Meakin et al. 1996). However, significant change in the mechanical loading or mechanical properties of such straight rods is required to achieve different deformation patterns. Such significant change in the mechanical characteristics of the rod may not be justifiable in human

✉ Saba Pasha
pashas@pennmedicine.upenn.edu

[1] Department of Mechanical Engineering and Applied Mechanics, University of Pennsylvania, Philadelphia, PA 19104, USA

[2] Perelman School of Medicine, University of Pennsylvania, Philadelphia, PA 19104, USA

Published online: 13 October 2020

spine. More recently, a reduced-order rod model for studying scoliosis has been proposed by Pasha (2019a). Using finite element analysis, this model simulates the spines as S-shaped slender elastic rods with varying curvatures while maintaining the same mechanical loading and mechanical properties for the rod (Pasha 2019a). This model showed the changes in the sagittal curvature of the spine itself can cause variation in the mechanical loading along the spine resulting in deformation modes that are similar to the scoliotic curve patterns (Pasha 2020). In the current study, we wish to determine the geometrical parameters that affect the deformation of such slender elastic rods, while mechanical loading and propertiese remain unchanged. One way to do this is by finite element simulation as was done previously by modeling the spine as a linear elastic material (Pasha 2019a). Repeating such finite element simulations while iterating over various initial shapes obtained by permutation of geometrical parameters is computationally prohibitive. To reduce computational cost, we developed a semi-analytical model using Kirchhoff equations (Meakin et al. 1996) to solve for the deformation given the initial geometry and loading on an S-shaped elastic rod (Neelakantan et al. 2020). The analytical model allows us to compute the deformed configuration of a rod subject to loads through a set of ordinary differential equations. The reduced computational complexity allows us to iterate over all permutations of the geometrical parameters describing the sagittal shape of the spine.

We simulate the curvature of the spine by two regions of constant curvature. We define the sagittal profile of the spine using 5 parameters shown in Fig. 1 which allows us to vary the shape of the sagittal curve systematically. Using this simplified geometry, we hypothesize that under the same mechanical loading and mechanical properties, the geometrical parameters–the two curvatures of the S-shaped rod, position of the inflection point and the slope of the curve at the lowest point with respect to the horizontal axis—can significantly impact the deformation of the rod. We hypothesize that the variations in the sagittal spinal alignment may modulate how the spinal deformity patterns in adolescent idiopathic scoliosis manifest.

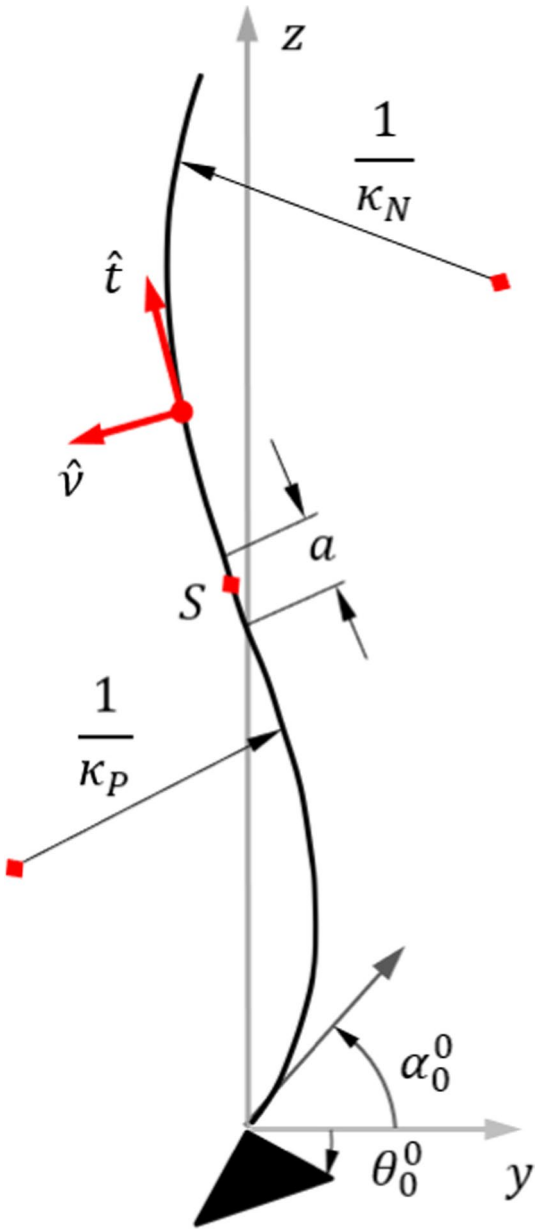

Fig. 1 Schematic of an S-shaped rod representing the spine. $\hat{\boldsymbol{\beta}}(s)$ vector of the Frenet–Serret frame points out of the plane. $\alpha_0 + \theta_0 = \pi/2$ and $\phi_0 = \pi/2$. Body force $f_z(s)$ acts in the negative $\mathbf{e}_z$ direction. The curvatures κ_P and κ_N, the position S of the inflection point and the angle θ_0 play important roles in determining the shape of the xy projection of the S-shaped rod when the loading and material properties are held fixed

2 Methods

Here, we describe an elastic rod model for the spine to investigate the effects of the different geometrical parameters. Since our goal is to focus on the geometrical parameters of the sagittal curvature, we will hold the bending modulus of our S-shaped rod fixed for all the simulations. We present a schematic in Fig. 1 to label the geometrical parameters.

The spine is modeled as an S-shaped elastic rod. The undeformed spine is assumed to rest on the $\mathbf{y} - \mathbf{z}$ plane with the base of the spine at the origin in the laboratory coordinate system given by $[\mathbf{e}_x \quad \mathbf{e}_y \quad \mathbf{e}_z]$. We define an arc length coordinate along the centerline s; a point located at s in the reference configuration moves in the deformed configuration to $\mathbf{r}(s) = x(s)\mathbf{e}_x + y(s)\mathbf{e}_y + z(s)\mathbf{e}_z$. The rod is then subject to a body force along the $-ve\ z$ direction which is caused due to the weight distribution of the upper

body. It is also subject to moments at the ends to simulate asymmetry in the body mass (Pasha et al. 2014).

The Frenet–Serret frame for the rod is $[\mathbf{t}(s) \quad \hat{\boldsymbol{\nu}}(s) \quad \hat{\boldsymbol{\beta}}(s)]$. $\hat{\mathbf{t}}(s)$ is the tangent vector, $\hat{\mathbf{t}}(s) = \frac{\mathrm{d}\mathbf{r}}{\mathrm{d}s}$. The rod is assumed in-extensible; hence, $\left|\hat{\mathbf{t}}(s)\right| = 1$. $\hat{\mathbf{t}}(s)$ can be expressed in the laboratory coordinate system as:

$$\begin{aligned}\hat{\mathbf{t}}(s) = &\cos\alpha(s)\cos\phi(s)\mathbf{e}_x + \cos\alpha(s)\sin\phi(s)\mathbf{e}_y \\ &+ \sin\alpha(s)\mathbf{e}_z,\end{aligned} \tag{1}$$

where α is the polar angle measured from the $x-y$ plane and ϕ is the azimuthal angle used in conventional spherical polar coordinates. $\hat{\boldsymbol{\nu}}(s)$ and $\hat{\boldsymbol{\beta}}(s)$ are the normal and binormal vectors, respectively, and they are computed using the Frenet–Serret equations:

$$\frac{\mathrm{d}\hat{\mathbf{t}}}{\mathrm{d}s} = \kappa\hat{\mathbf{n}}, \qquad \frac{\mathrm{d}\hat{n}}{\mathrm{d}s} = -\kappa\hat{\mathbf{t}} + \tau\hat{\boldsymbol{\beta}}, \qquad \frac{\mathrm{d}\hat{\boldsymbol{\beta}}}{\mathrm{d}s} = -\tau\hat{\mathbf{n}}. \tag{2}$$

The curvature $\kappa(s)$ and the torsion $\tau(s)$ of the rod are obtained from the above equations (Nizette and Goriely 1999). This completes the kinematic description of the rod.

2.1 Mechanics

Next, we present the equilibrium equations for the rod. We begin with the conservation of linear momentum (Antman 2006; Audoly 2010),

$$\frac{\mathrm{d}n_x}{\mathrm{d}s} = 0, \tag{3}$$

$$\frac{\mathrm{d}n_y}{\mathrm{d}s} = 0, \tag{4}$$

$$\frac{\mathrm{d}n_z}{\mathrm{d}s} + f_z(s) = 0 \tag{5}$$

where $\mathbf{n}(s) = [n_x(s) \quad n_y(s) \quad n_z(s)]$ is the internal force in the rod. $\mathbf{f} = f_z(s)\mathbf{e}_z$ is the body force on the rod and is directed only along the $\mathbf{e}_z$ direction due to gravity. For $f_z(s)$, we use the values found in Pasha et al. (2014). The rod is assumed in-extensible; hence, there is no constitutive law for $\mathbf{n}(s)$. $\mathbf{n}(s)$ must be determined as part of the solution of the boundary value problem for the rod. We use Eqs. (2) and (3) to get

$$n_x(s) = n_x^0, \qquad n_y(s) = n_y^0. \tag{6}$$

Since there are no forces in the $\mathbf{e}_x$ and $\mathbf{e}_y$ directions, $n_x^0 = n_y^0 = 0$. The conservation of angular momentum of the rod states that

$$\begin{aligned}\frac{\mathrm{d}m_x}{\mathrm{d}s} + (\hat{t}\times n)_x + l_x = 0,\\ \frac{\mathrm{d}m_y}{\mathrm{d}s} + (\hat{t}\times n)_y + l_y = 0,\\ \frac{\mathrm{d}m_z}{\mathrm{d}s} + (\hat{t}\times n)_z + l_z = 0,\end{aligned}$$

where $\mathbf{m}(s) = [m_x(s) \quad m_y(s) \quad m_z(s)]$ is the internal moment in the rod in the laboratory frame and $\mathbf{l}$ is the body moment per unit length. We set $\mathbf{l} = \mathbf{0}$ in this work. Since $n_x = n_y = 0$, the balance of angular momentum becomes:

$$\frac{\mathrm{d}m_x}{\mathrm{d}s} + n_z\sin\phi\cos\theta = 0, \tag{7}$$

$$\frac{\mathrm{d}m_y}{\mathrm{d}s} - n_z\cos\phi\cos\theta = 0, \tag{8}$$

$$\frac{\mathrm{d}m_z}{\mathrm{d}s} = 0. \tag{9}$$

We get $m_z = T$ from Eq. (9), a constant which we compute from torque boundary condition applied at $s = 0$.

The internal moment can be written in the Frenet frame as $\mathbf{m} = m_t\hat{\mathbf{t}} + m_\nu\hat{\boldsymbol{\nu}} + m_\beta\hat{\boldsymbol{\beta}}$ which is convenient if we use the following simple constitutive relation:

$$\mathbf{m} = K_b(s)(\kappa - \kappa^0(s))\hat{\boldsymbol{\beta}} + K_t(s)(\kappa_3 - \kappa_3^0)\hat{\mathbf{t}}, \tag{10}$$

where $K_b(s)$ and $K_t(s)$ are the bending and twisting moduli of the elastic rod, respectively. The curvature functions in the stress free state are given by $\kappa^0(s)$ and $\kappa_3^0(s)$, respectively. We assume $\kappa_3^0 = 0$. This constitutive law is a special case of a general form given by $\mathbf{m} = K_b(\kappa_1 - \kappa_1^0)\mathbf{d}_1 + K_b(\kappa_2 - \kappa_2^0)\mathbf{d}_2 + K_t(\kappa_3 - \kappa_3^0)\mathbf{d}_3$ where $[\mathbf{d}_1(s) \quad \mathbf{d}_2(s) \quad \mathbf{d}_3(s)]$ is a material frame that convects with the arc-length coordinate s.

Plugging this constitutive law into the conservation of angular momentum and considering the component along the $\hat{\mathbf{t}}$ direction only gives (Antman 2006; Audoly 2010)

$$\frac{\mathrm{d}K_t}{\mathrm{d}s}(\kappa_3(s) - \kappa_3^0(s)) + K_t(s)\left(\frac{\mathrm{d}\kappa_3}{\mathrm{d}s} - \frac{\mathrm{d}\kappa_3^0}{\mathrm{d}s}\right) = 0. \tag{11}$$

If we define $K_t(s)(\kappa_3(s) - \kappa_3^0(s)) = m_3(s)$, then Eq. (11) shows that $\frac{\mathrm{d}m_3}{\mathrm{d}s} = 0$ or $m_3 = const$. We also set $K_b(s)$ as constant since our focus is on the effects of the geometrical parameters. Then, from the constitutive law, we can write the moment in the laboratory frame as

$$\begin{aligned}m_x = &K_b\frac{\kappa(s) - \kappa^0(s)}{\kappa(s)}\left[-\phi'\cos\phi\sin\alpha\cos\alpha + \alpha'\sin\phi\right] \\ &+ m_3\cos\phi\cos\alpha,\end{aligned} \tag{12}$$

$$m_y = K_b \frac{\kappa(s) - \kappa^0(s)}{\kappa(s)} \left[-\phi' \sin\phi \sin\alpha \cos\alpha - \alpha' \cos\phi \right] + m_3 \sin\phi \cos\alpha, \tag{13}$$

$$m_z = K_b \frac{\kappa(s) - \kappa^0(s)}{\kappa(s)} \phi' \cos^2\alpha. + m_3 \sin\alpha. \tag{14}$$

The elimination K_b, $\kappa^0(s)$ and $\kappa(s)$ from the above gives:

$$m_x \cos\phi + m_y \sin\phi = -m_z \tan\alpha + \frac{m_3}{\cos\alpha}, \tag{15}$$

$$(m_x \sin\phi - m_y \cos\phi)\phi' = \frac{m_z - m_3 \sin\alpha}{\cos^2\alpha} \alpha'. \tag{16}$$

Then, we solve Eq. (15) to get

$$\sin\alpha = \frac{m_3 m_z \pm P\sqrt{P^2 + m_z^2 - m_3^2}}{P^2 + m_z^2}, \tag{17}$$

$$P = m_x \sin\phi + m_y \cos\phi, \tag{18}$$

where we determine the solution branch from α_0. We compute $\phi'(s)$ using Eq. (16) to get

$$\phi' = \frac{m_z - m_3 \sin\alpha}{K_b(s) \cos^2\alpha} \pm \frac{\kappa^0(s)}{\cos\alpha} \frac{1}{\sqrt{1 + \cos^2\alpha \frac{(m_x \sin\phi - m_y \cos\phi)^2}{(m_z - m_3 \sin\alpha)^2}}}, \tag{19}$$

where the $\pm$ sign is dependent on the sign of $\phi'(s)$.

Finally, the deformed curve can be determined using

$$\frac{dx}{ds} = \cos\phi \cos\alpha, \tag{20}$$

$$\frac{dy}{ds} = \sin\phi \cos\alpha, \tag{21}$$

$$\frac{dz}{ds} = \sin\alpha. \tag{22}$$

This along with Eqs. (5), (7), (8) and (19) forms the governing equations of the system along with the boundary conditions given by:

$$\begin{aligned} &n_z(0) = n_{z_0}, \quad m_x(0) = m_{x_0}, \quad m_y(0) = m_{y_0}, \\ &\phi(0) = \pi/2, \quad x(0) = 0, \quad y(0) = 0, \quad z(0) = 0, \end{aligned} \tag{23}$$

where n_{z_0} is the weight of the upper body and m_{x_0} and m_{y_0} are used to account for the loading asymmetry experienced by a scoliotic spine.

2.2 Phase plot

Now, we will use the above model to study the effects of the different geometrical parameters of the curved rod. K_b is set to an arbitrary constant. We will simplify $\kappa^0(s)$ using the following function:

$$\kappa^0(s) = \frac{\kappa_P + \kappa_N}{2} + \frac{\kappa_P - \kappa_N}{2} \tanh\left(\frac{s - S}{a}\right), \tag{24}$$

where S is the point of inflection of the rod and a is the distance over which the curvature of the rod goes from κ_P to κ_N. κ_N/κ_P are the curvatures of the lower/upper portion of the rod (above and below the inflection point, respectively).

We will focus on the effects of varying κ_P, κ_N, S, a and θ_0. The range of values for these parameters used in this study are given in Table 1. To reduce the data space, we study the parameters that cause the largest change in deformations. We restrict θ_0 to the three major values found in clinical studies (Pasha and Baldwin 2019b).The range of values for κ_P, κ_N, S and a are based on maximum and minimum values of these parameters in Pasha et al. (2019a) who investigated the geometrical shapes of spines of patients with adolescent idiopathic scoliosis. For a range of a (0.01–0.1), we did not observe significant changes in deformation when we varied a over this range. So, we keep a fixed in all our computations and focus on the remaining four geometrical parameters.

We have chosen the moments in Table 1 based on work in Neelakantan et al. (2020). Neelakantan et al. had solved an inverse problem to deduce the bending modulus $K_b(s)$ and the moments m_z, m_3, etc., to match clinically observed scoliotic spine shapes under given loading due to the weight of organs. The values of m_z, average K_b and their ratio m_z/K_b are given in Table 2. We are interested in the ratio $\frac{m_z}{K_b}$ because it is a curvature and curvatures of scoliotic spines are known, while no experimental measurement of K_b or m_z, m_3, etc., is available. Table 2 shows that the ratio $\frac{m_z}{K_B}$ varies from $-0.11\ \mathrm{m}^{-1}$ to $0.1\ \mathrm{m}^{-1}$. Recall that m_z is used to simulate a torsion following

Table 1 Parameter values used to investigate the effects of geometry

$\kappa_P\,(\mathrm{m}^{-1})$	$\kappa_N(\mathrm{m}^{-1})$	S (m)	θ_0 (°)	a (m)	$K_b(\mathrm{Nm}^{-2})$	m_z (Nm)	m_3 (Nm)	$m_x(0)$ (Nm)
0.1–5	0.1–5	0.3–0.8	31°, 37°, 44°	0.01	10	− 2	0	− 8

Moment and stiffness values are the same for all rods studied. The width of the region over which the curvature changes from κ_N to κ_P is a. a has little effect on the phase diagrams that follow, so it is also the same for all rods studied

Table 2 m_z and average K_b values from Neelakantan et al. (2020)

Case	m_z (Nm)	Avg (K_b) (Nm^2)	m_z/K_b (m^{-1})
Case 1	− 11.32	158.61	− 0.07
Case 2	21.72	216.95	0.1
Case 3	16.52	302.75	0.05
Case 4	− 25.24	269.27	− 0.09
Case 5	− 24.49	212.49	− 0.11

(Pasha 2019a), although it is clear that pure gravity loads in the z-direction alone cannot give rise to an m_z. We have set m_3 to zero to ease calculation and understanding of the system because it also causes torsion which is already taken into account by a nonzero m_z. The value of $m_x(0)$ is chosen such that the deformation in the axial view is of the same order as in Neelakantan et al. [compare Fig. 10 of this manuscript with Fig. 1 in Neelakantan et al. (2020)]. Since the moment values are constrained by Eq. (16) and we have set $m_x(0)$, m_z and m_3, m_y is already fixed and does not need to be specified. With this rationale for our choice of parameters in Table 1, our goal is to show how geometrical parameters of an S-shaped rod produce different shapes, which resemble shapes of scoliotic spines, even when loading and material properties of the rod are fixed.

2.3 Uprightness

To ensure the deformed state of the rod is physiologically acceptable, we restrict the values of the parameters such that the initial configuration of the spine remains upright. The shape of the spine is assumed to lie in the $\mathbf{y}-\mathbf{z}$ plane in the absence of loads. Hence, when $\phi(s)=\pi/2$ we can compute the initial curve from $\kappa^0(s)$ using the following system of ODEs

$$\kappa(s)=\frac{\mathrm{d}\alpha}{\mathrm{d}s}=\kappa^0(s), \tag{25}$$

$$\frac{\mathrm{d}y}{\mathrm{d}s}=\cos\alpha, \tag{26}$$

$$\frac{\mathrm{d}z}{\mathrm{d}s}=\sin\alpha. \tag{27}$$

We limit the $\mathbf{y}$ displacement of the top of the S-shaped rod to 20% of the $\mathbf{z}$ displacement in the initial configuration to filter out unrealistic shapes where there is a large displacement between the head and pelvis, i.e., the two ends of the rod. This constraint boils down to

$$|y(L)|<0.2\,|z(L)|. \tag{28}$$

Now we apply the analytical model to find the deformation over the range of parameters. As shown previously by Pasha et al. (2019a), the most common curve types in scoliosis deform in a loop or Lemniscate shape in the axial plane ($\mathbf{x}-\mathbf{y}$ plane). We classify the deformed shapes as loop or Lemniscate based on the number of points of intersection the curve in the $\mathbf{x}-\mathbf{y}$ projection has with the line segment joining the two end points of the curve. The curve is classified as a loop shape if the line segment does not intersect the curve and as a Lemniscate shape if the line segment intersects with the curve at least once (we exclude the intersection at the end points). We perform this check over the range of parameters given in Table 1.

We create a scatter plot of points in the data space which satisfies the Lemniscate condition using κ_P, κ_N and S as the axes of the plot. The boundary points are filtered and surfaces are fit to the points. A polynomial fit is used to separate the regions into loop and Lemniscate shapes. A similar procedure is followed for points satisfying the upright condition and a polynomial fit is used to create surfaces to separate regions where the undeformed rod is upright from those where it is not.

For each θ_0, we plot all the initial configurations that deform into loop and Lemniscate shapes, respectively, along with the average curve for each case. The equations of the surfaces for the Lemniscate condition along with the coefficient of determination of the fit ($\boldsymbol{R^2}$) are given in Table 4 in appendix. The resulting three surface plots at the three θ_0 values appear in "Results" section.

3 Results

Figure 2 presents the loop–Lemniscate classification regions and the condition of uprightness in the data space. We see in Fig. 2a that two surfaces divide the volume of interest into three parts comprising of two loop regions and one Lemniscate region. We label the loop region with low κ_P and S as "Loop2" and the other region as "Loop1." Only variable ranges bounded by both uprightness surfaces and loop–Lemniscate classification surfaces are presented in the following sections. The different regions are classified accordingly and serve as a reference when we consider both conditions together in the following plots.

Next, we present the combined surface plots in Fig. 3. We present the surface plots for 3 angles—31°, 37° and 44°. The surfaces span the entire parameter space, so that we can visualize any trends that develop in the region of interest. We have included the equations of the surfaces and the fit information in Table 4 of appendix. We have also presented the range of values in Table 3. We also present the equations for the uprightness check surface (yellow surface) in Table 5 of appendix.

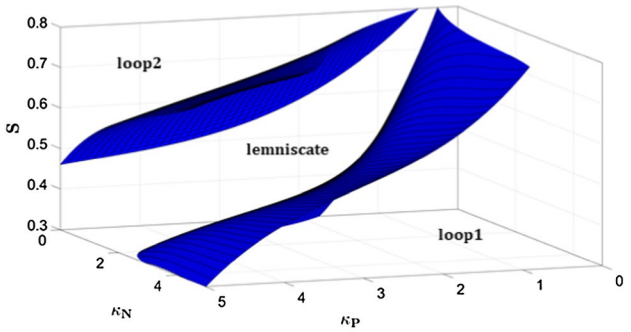

(a) loop-lemniscate classification surfaces

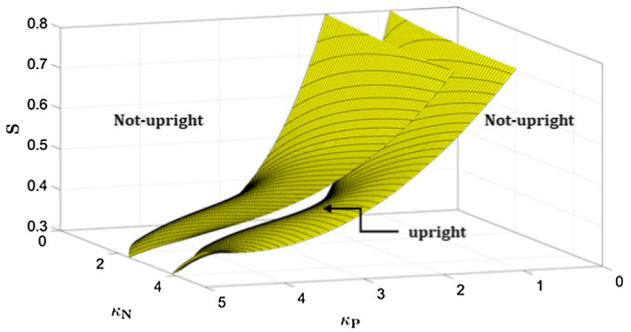

(b) Uprightness classification surfaces.

Fig. 2 Representative classification surfaces with regions marked. When the line joining the end points of the xy projection does not intersect the xy projection of the curved rod, then we call it a loop; when it intersects once, then we call it a Lemniscate. When $|y(L)| < 0.2|z(L)|$, then the curved rod is said to represent an upright spine

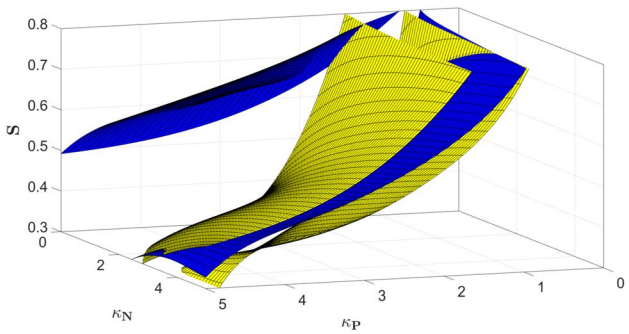

(a) θ_0=31°

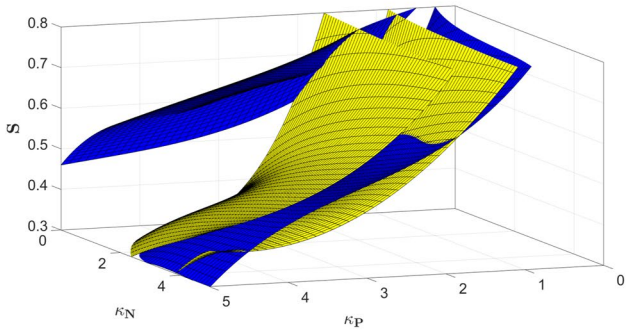

(b) θ_0=37°

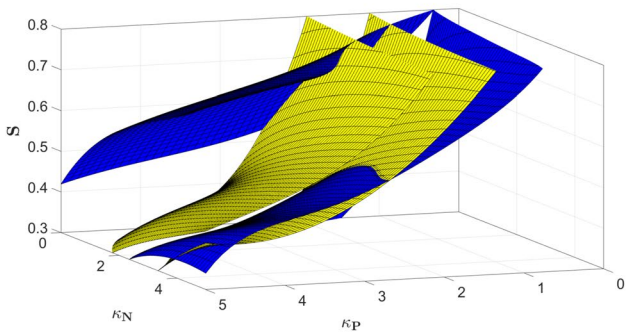

(c) θ_0=44°

Fig. 3 Loop and Lemniscate regions for each case of θ_0. The space between the blue surfaces reduces with increasing θ_0. The yellow surfaces shift left (toward increasing κ_P) with increasing θ_0

Figure 2b shows that the range of admissible κ_P values that satisfy the uprightness condition is smaller than the range of κ_N values for each S. Recall that the range of a is also very small and it has minimal effect on the classification of deformation patterns.

To show that the phase plots in Fig. 2a, b are typical and not an isolated result of our choice of parameters in Table 1, we give phase plots for different choices of loading in Figs. 4 and 5. The effect of m_z on the loop–Lemniscate surface is shown in Fig. 4 by taking $m_z = -1$ Nm and 1 Nm and $\theta_0 = 37°$ (while keeping all other parameters the same as given in Table 1). Our choice of these m_z values is based on Table 2 in which $-0.11 < \frac{m_z}{K_b} < 0.1\text{m}^{-1}$. Similarly, a phase plot with m_3 = -1Nm with all other parameters as given in Table 1 is shown in Fig. 5. These phase plots look qualitatively similar to other such plots presented before, confirming that they are typical. We have used the parameters in Table 1 because they produce phase plots that are visually clear, but the qualitative conclusions of this paper do not depend on the particular choice of parameters in Table 1.

We present the shape of the initial configurations that lead to loop and Lemniscate shapes in the deformed configuration in Fig. 6. The initial shape of the curve (black line) along with the range of the curves (shaded area) for each θ_0 is shown in Fig. 6. The corresponding sagittal profile values are presented in Table 3. As shown in both Fig. 6 and Table 3, the position of the inflection point is the highest, closer to the top, in Loop1 and decreases in Lemniscate and Loop2 cases. However, the changes in the inflection point position within each case as the θ_0 changes are small. Both κ_P and κ_N are the smallest in Loop1 cases and highest in Loop2 cases, suggesting a more flat sagittal profile in Loop1 patients compared to the Lemniscate and Loop2 cases.

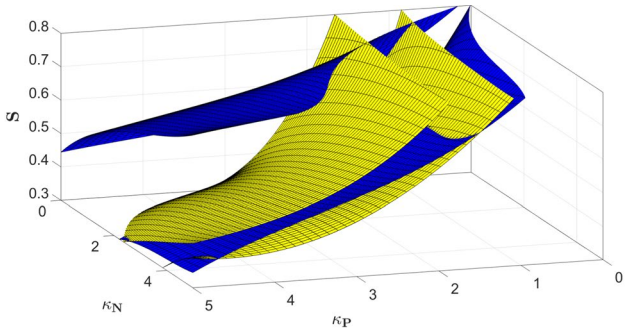

(a) m_z=-1Nm

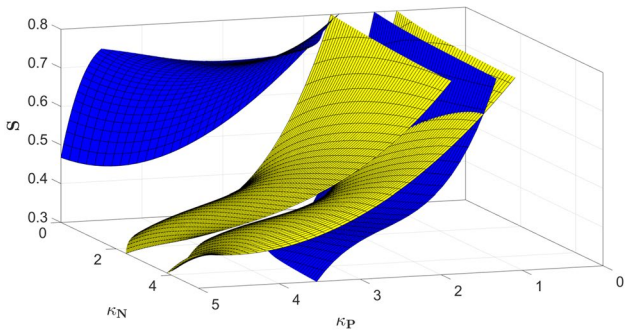

(b) m_z=1Nm

Fig. 4 Effect of varying m_z while keeping the remaining parameters fixed as given in Table 1. $\theta_0 = 37°$. The two plots cover the two extreme values of $\frac{m_z}{K_b}$ in Table 2

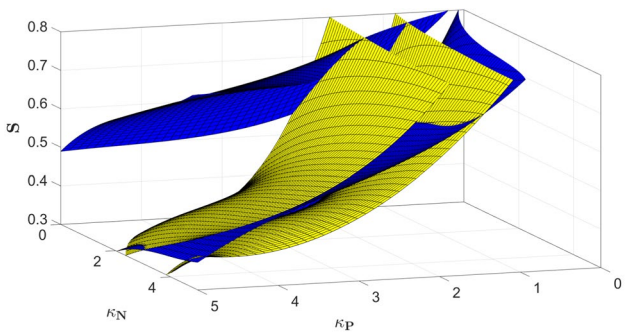

Fig. 5 Effect of nonzero $m_3 = -1$Nm while keeping other parameters fixed as given in Table 1. $\theta_0 = 37°$

4 Discussion

We analyzed the deformation patterns of S-shaped elastic rods to investigate the role of geometrical parameters of the sagittal spine on the deformity patterns seen in scoliotic spines. Our results show that under the same initial bending and torsion loading, informed by our previous work in Neelakantan et al. (2020), an S-shaped elastic rod deforms in three distinct configurations (deformation modes), presented as Loop1, Lemniscate and Loop2 (Fig. 2a). We also determined specific geometrical characteristics of these S-shaped rods leading to these three deformation patterns (Table 3).

Since the moments acting on the spine and its bending modulus have not been experimentally measured, but its curvatures can be estimated, we perform our analysis for a particular choice of $\frac{m_z}{K_b}$. A nonzero m_z is needed because it represents a torsional load that ultimately causes the out-of-plane deformation of our S-shaped rod mimicking the deformation seen in scoliotic patients. The other loading parameters used here are chosen such that the magnitude of the deformation is of the same order as in Neelakantan et al. (2020) which was determined using clinical data. We show that the phase plots demarcating regions of loop and Lemniscate projections look qualitatively similar to the 3D scoliotic patterns seen in Pasha et al. (2019a) irrespective of the choice of loading parameters, so we keep the loading fixed in this paper and focus instead on the geometrical parameters of the S-shaped rod.

The sagittal curvature of the spine in idiopathic scoliosis has been hypothesized to be a mechanical factor leading to the spinal deformity development (Chu et al. 2008; de Reuver et al. 2018; Janssen et al. 2011; Kouwenhoven et al. 2006; Pasha et al. 2019b, c; Schlösser et al. 2014). However, specific characteristics of the sagittal curve that determine the deformity patterns of the spine are not known. Here, our analysis of S-shaped elastic rods showed that without any assumption about the mechanical properties of the different sections of the spine, geometrical details of the vertebral body or properties of the intervertebral disk, three distinct modes of deformation can be identified for a curved elastic rod under bending and torsion: two loops and one Lemniscate. These deformation modes, which are related to the geometrical parameter of the rod (Table 3), were also observed in the most common scoliotic curve types (Lenke 1 and Lenke 5) (Duong et al. 2006; Pasha et al. 2019a). Lenke 1 scoliosis, which manifests as a deformity in the thoracic spine, was shown to have axial deformation patterns as seen in Loop1 and Lemniscate. On the other hand, Lenke 5 scoliosis had loop-shaped deformity patterns as was seen in Loop2 cases. Moreover, the Lenke 1 cases with loop-shaped axial projection were shown to have a higher inflection point compared to the Lenke 1 with Lemniscate axial projection and Lenke 5 patients (Pasha et al. 2019a) (as shown in Fig. 7). Although we used the result of our previous study on Lenke 1 patients to determine the mechanical loading of the spine (Neelakantan et al. 2020), our analysis here was able reproduce the deformation patterns that are observed in Lenke 5 just by changing the sagittal curvature parameters. This clinical observation matched the simulation results as

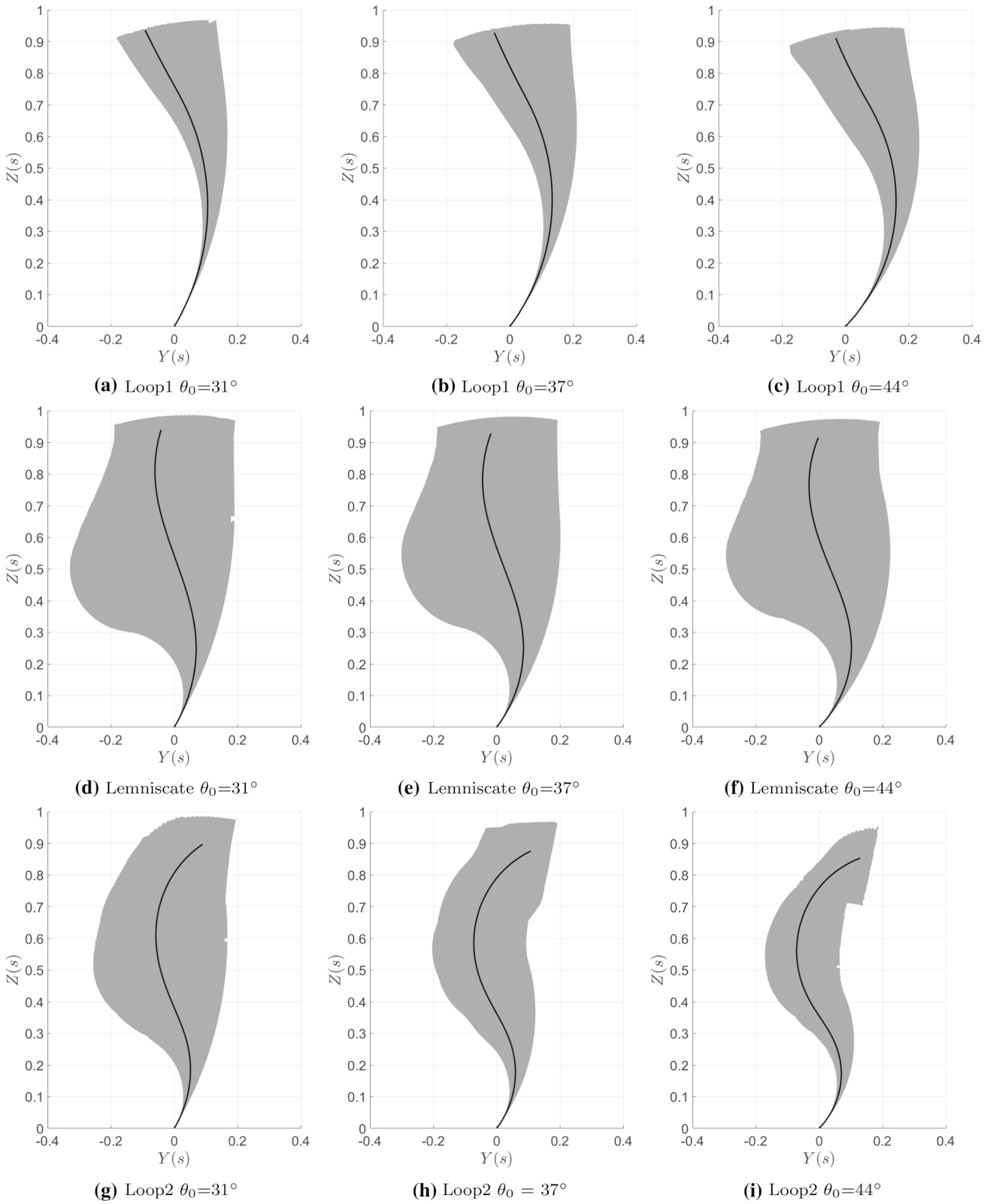

(a) Loop1 θ_0=31° **(b)** Loop1 θ_0=37° **(c)** Loop1 θ_0=44°

(d) Lemniscate θ_0=31° **(e)** Lemniscate θ_0=37° **(f)** Lemniscate θ_0=44°

(g) Loop2 θ_0=31° **(h)** Loop2 θ_0 = 37° **(i)** Loop2 θ_0=44°

Fig. 6 Initial configuration to get loop and Lemniscate shapes for each case of θ_0. The line is the average curve, and the gray region corresponds to the range

Table 3 Average and range of the geometrical parameter values describing the sagittal profile for Loop1, Lemniscate and Loop2 cases

Case	θ_0	κ_P		κ_N		S	
Loop1	31°	**1.36**	[0.85 : 1.60]	**0.32**	[0.10 : 0.85]	**0.81**	[0.70 : 0.80]
	37°	**1.50**	[0.95 : 1.90]	**0.44**	[0.10 : 1.45]	**0.80**	[0.65 : 0.80]
	44°	**1.75**	[1.20 : 2.30]	**0.62**	[0.10 : 2.05]	**0.80**	[0.60 : 0.80]
Lemniscate	31°	**2.06**	[0.75 : 5.00]	**1.75**	[0.10 : 5.00]	**0.56**	[0.30 : 0.80]
	37°	**2.71**	[1.10 : 5.00]	**2.50**	[0.45 : 5.00]	**0.55**	[0.30 : 0.80]
	44°	**2.74**	[1.25 : 5.00]	**2.12**	[0.10 : 5.00]	**0.55**	[0.30 : 0.80]
Loop2	31°	**2.78**	[0.85 : 5.00]	**2.72**	[0.10 : 5.00]	**0.41**	[0.30 : 0.80]
	37°	**4.35**	[3.10 : 5.00]	**4.19**	[2.75 : 5.00]	**0.40**	[0.30 : 0.45]
	44°	**4.03**	[2.55 : 5.00]	**3.18**	[1.05 : 5.00]	**0.40**	[0.30 : 0.50]

The parameter values of the average curve is in bold. The range of values are reported within square brackets

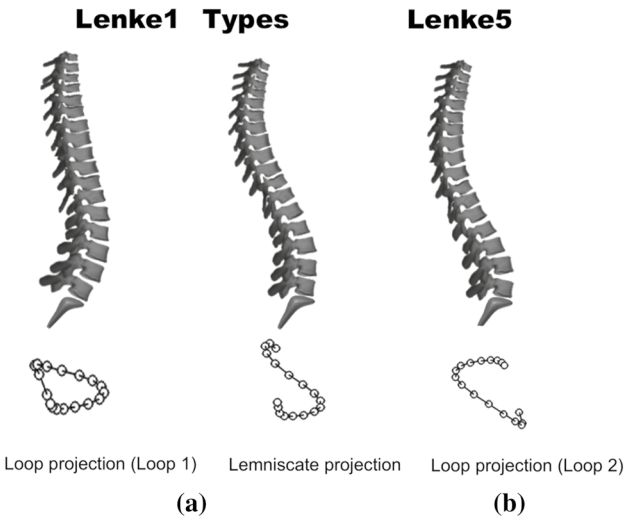

Fig. 7 Schematics of the sagittal profiles in Lenke 1 scoliosis with loop (**a**) and Lemniscate (**b**) axial projection and Lenke 5 scoliosis with loop-shaped axial projection

given in Table 3. Our reduced-order model was able to differentiate between these curve types providing evidence that geometry alone can give rise to different scoliosis-like deformations under the same loading and material properties.

Figure 6 and Table 3 show that the average initial configurations that produce loop and Lemniscate projections are different. κ_P and κ_N that produce a particular projection (loop or Lemniscate) increase with an increase in θ_0 in most cases; exceptions are κ_N in Lemniscate and Loop2. We see that $\kappa_P \approx \kappa_N$ in these three cases. The parameter values are different for the two loop regions. Table 3 shows that intermediate values of κ_P, κ_N and S lead to the top view of the deformation being Lemniscate shape. Low or high values of these parameters leads to the loop shape. Our results show that we can predict the deformation case based on a limited number of geometrical parameters.

Our analysis further investigated the mechanical loading of the S-shaped rod in the three deformation modes. As shown in Figs. 8 and 9, although the external loading

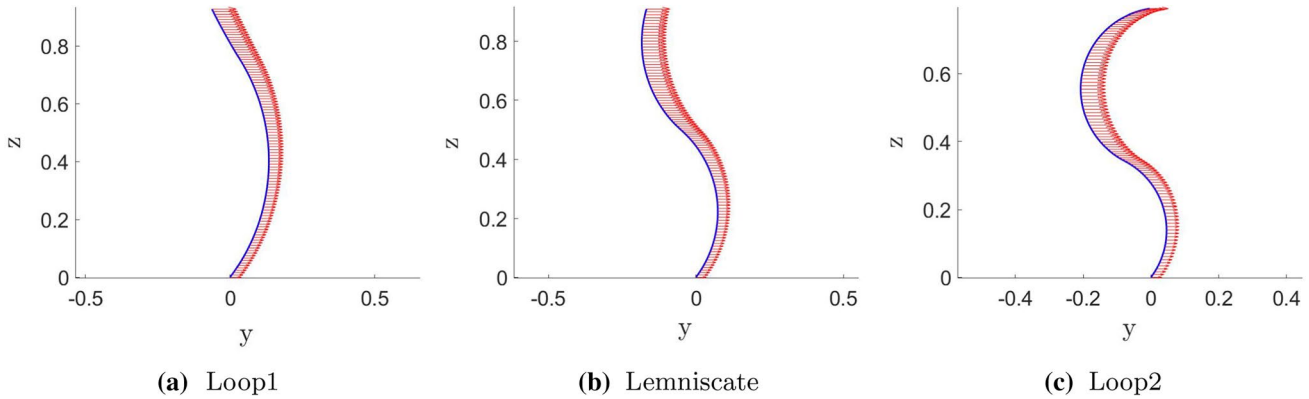

Fig. 8 Sagittal view of the initial configuration of the 37° average curve in Fig. 6. ($m_y(s)$ plotted as red vectors). We see how changes in initial sagittal geometry can affect axial view of the deformed configuration

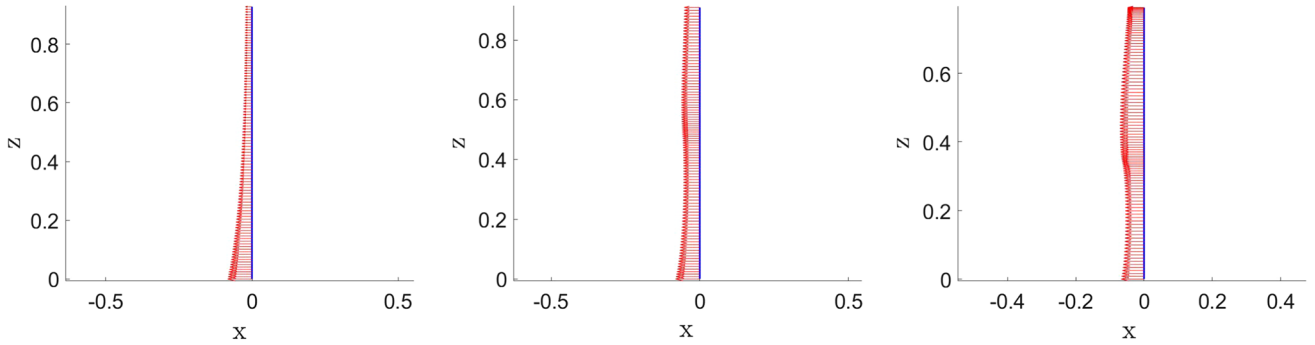

(a) Loop1 **(b)** Lemniscate **(c)** Loop2

Fig. 9 Frontal view of the initial configuration of the 37° average curve in Fig. 6. ($m_x(s)$ plotted as red vectors)

(gravity and torsion) and mechanical properties of the rods are the same, the moment distribution along the rod varies in the **y**–**z** and **x**–**z** planes resulting in different deformation patterns as shown in Fig. 10. The geometry affects the final deformations because the moments in the rod depend on α and ϕ as seen in Eqs. (7) and (8). m_y causes primarily bending deformations in the **x-z** plane, while m_z causes twisting deformations, bringing the rod out of the **y**–**z** plane. We see that $m_x(s)$ is negative and the rod bends toward **+ve y-**axis in all three cases. m_x changes along the spine in Loop1, but does not seem to affect the other cases as the deformation in the **y-z** projection can be explained by the effects of $m_x(s)$. The reason m_z does not affect the deformation **y**–**z** projection is due to the difference in magnitude between $m_x(s)$ and $m_z(s)$. However, when both of these moments are nonzero it is difficult to qualitatively explain the deformation of the rod from a knowledge of their magnitudes. As shown in Fig. 10, the shape in the **x**–**y** projection is predominantly determined by m_z. Note that $m_y(s)$ is positive in all three cases of Fig. 8, and the axial projection of the three cases follows the same qualitative trend. In particular, the rod deflects toward the **-ve x-**axis for small s and then bends toward the **+ve x-**axis for larger s. (In the Loop1 case, this trend is not as obvious as the other two cases, but the rod begins to bend toward the **+ve x-**axis for larger s.) Thus, the sign of the m_y moment and the deformation are correlated. The deformed shape of the sagittal curves is presented in appendix. It can be seen that the relative position of the inflection point varies between the groups, i.e., Loop1 being the highest and Loop2 the lowest with respect to the horizontal axis as was seen prior to the deformation holds true in the deformed shape of the spine (Appendix Fig. 11).

As the mechanical loading on the spine results in the 3D deformation of the spine in scoliosis, the changes in the stress/strain patterns on the growth plate can impact the osteoblast function in the vertebral body and disk properties resulting in permanent changes in the functional units of the spine. As proposed before by Stokes et al. (1998), such changes that induce vertebral wedging result in a vicious cycle that further causes curve development. Although a possibility, we have not tested the primary or secondary cause of the vertebral asymmetry in this paper, yet we showed that the sagittal curvature of the spine impacts the mechanical loading of the spine; thus, geometry could possibly cause increased loading in different sections of the spine for patients with different sagittal curvatures (Pasha 2019a). This observation was also shown in our previous work in which abnormal bone growth was dependent on

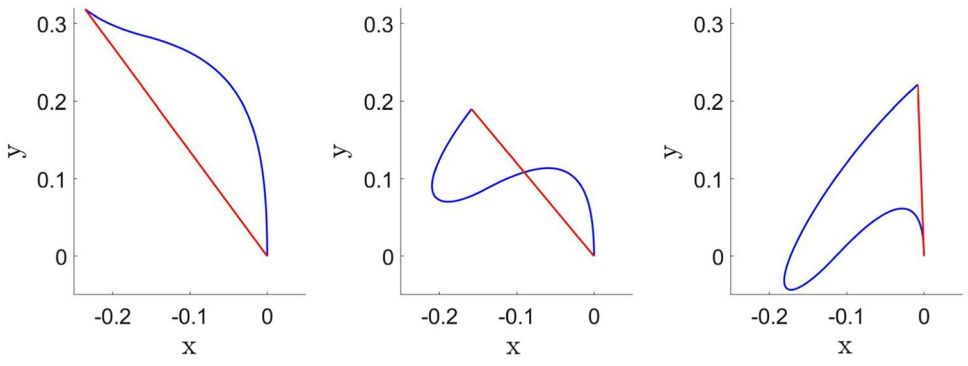

(a) Loop1 **(b)** Lemniscate **(c)** Loop2

Fig. 10 Axial view of the deformed configuration of the 37° average curve in Fig. 6. Red line segment connects end points to show loop/Lemniscate classification

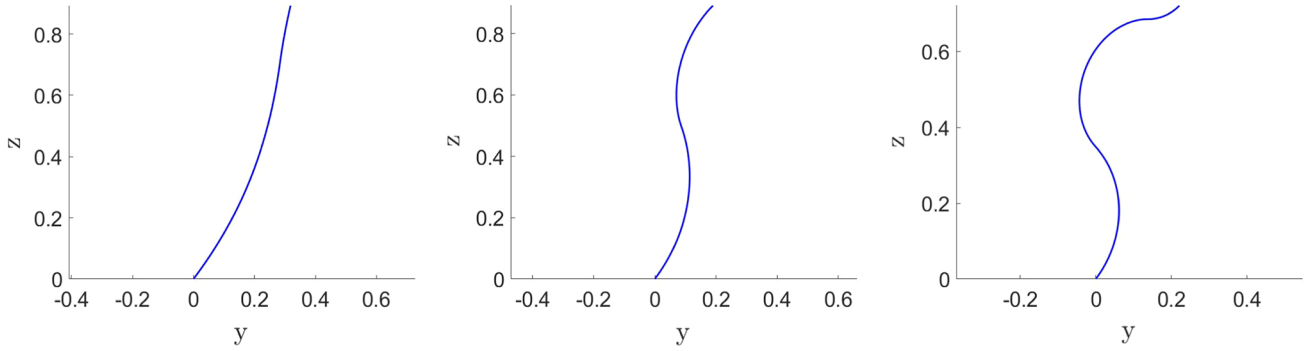

(a) Loop1 **(b)** Lemniscate **(c)** Loop2

Fig. 11 Sagittal view of the deformed configuration of the 37° average curve in Fig. 8

curve development and did not occur equally at all vertebral levels (Pasha et al. 2019b). As such, our model did not intend to include abnormal growth as a mechanism that initiates deformation. Instead, our model was developed to explain how changes in the sagittal curvature can impact the biomechanical loadings and consequently the deformation patterns.

In this study, we fixed the mechanical loading and mechanical properties of the S-shaped rod and observed scoliosis-like deformations only as a function of the geometrical differences between the sagittal curvatur1992es. In a straight rod, as previously has been proposed as a model of scoliosis (Crisco and Panjabi 1992; Crisco et al. ; Goto et al. 2003; Lucas and Boris 1961; Meakin et al. 1996), doing so will not produce scoliosis-like deformations. Different scoliotic patterns in a straight rod only can be produced by assuming significant variations in the compressive load or mechanical properties of the spine in patients with scoliosis. As such, we do not believe that a straight rod can produce scoliosis-like deformities as a result of constant axial compression and axial torsion. The sagittal curve, as opposed to the straight rod, can cause variation in the location of the maximum/minimum moments along the spine. Thus, the curvatures and position of the inflection point, among other variables related to the S-shaped curvature of the spine, impact the mechanical loading of the spine. This is obviously not the case in an straight rod. Yet, causation of scoliosis, i.e., development of large 3D curves is multifactorial and having a specific sagittal curve alone may not result in scoliosis.

Finally, it is important to point out some limitations of our analysis. We chose a nonzero m_z to induce 3D deformation and break the symmetry of the system (Pasha 2019a) even though gravity loading in the z-direction alone cannot produce such a moment. The change in the position of the center of mass at the onset of scoliosis curve development was assumed to result in the tendency of the sagittal curve rotation in one direction in a majority of AIS patients. In a living person, in this case a fast-growing child, growth may induce this off-plane deformation and the direction of such deformation may be dictated by the trunk mass asymmetry of the trunk, explaining why a majority of the curves are right thoracic and left lumbar. However, growth is not taken into account in our model. A nonzero torsional moment m_3 could also have caused off-plane deformation of our S-shaped rod; we did not pursue these possibilities here because the loading parameters used are sufficient to support our hypothesis that geometrical parameters alone can produce scoliosis-like deformation patterns of an S-shaped rod. Our model has other limitations. It assumes a constant bending modulus K_b even though (Neelakantan et al. 2020) had shown that it may vary as function of position in the spine and even among different people (Pasha et al. 2014b). Furthermore, the values of the bending modulus and the moments m_z, m_x, etc., have not been measured in experiments, so they cannot be directly verified. However, the values used here do produce deformations (in the axial projections) and curvatures that are in the same range as those in Neelakantan et al. (2020).

5 Conclusion

By changing the geometry of an S-shaped elastic rod, we determined three different deformation patterns while loading and material properties of the rod were held fixed. The deformation patterns were related to the position of the inflection point of the S-shaped rod and the curvature of the rod above and below the inflection point. These parameters change slightly as the base angle of the rod changes within each deformity pattern group. These curve characteristics relate to the sagittal curvature of the spine in the most common scoliotic curve types and they produce axial projections that mimic those seen in scoliotic patients.

Table 4 Equations of the loop–Lemniscate classification surfaces (Fig. 3 blue surface) for the 3 cases in along with the coefficient of determination

θ_0	Surface ($f(x, y)$)	R^2
31°	$-0.00215\,x^3 - 0.00384\,x^2\,y + 0.0369\,x^2 + 0.00448\,x\,y^2 + 0.00775\,x\,y - 0.222\,x + 0.00162\,y^3 - 0.0388\,y^2 + 0.153\,y + 0.946$	0.9953
	$-0.00161\,x^5 + 0.0279\,x^4 - 0.00136\,x^3\,y^2 + 0.0199\,x^3\,y - 0.201\,x^3 + 0.00739\,x^2\,y^2 - 0.108\,x^2\,y + 0.728\,x^2 - 0.0146\,x\,y^2 + 0.22\,x\,y - 1.39\,x - 0.00677\,y^4 + 0.0398\,y^3 - 0.112\,y^2 + 0.108\,y + 1.32$	0.9983
37°	$-0.00328\,x^3 - 0.00293\,x^2\,y + 0.0458\,x^2 + 0.0041\,x\,y^2 + 0.00124\,x\,y - 0.236\,x + 0.00265\,y^3 - 0.0462\,y^2 + 0.188\,y + 0.906$	0.9930
	$-0.0109\,x^3 - 0.00603\,x^2\,y + 0.131\,x^2 - 0.00153\,x\,y^2 + 0.0415\,x\,y - 0.56\,x + 0.00344\,y^3 - 0.0364\,y^2 + 0.126\,y + 0.934$	0.9912
44°	$-0.00501\,x^3 + 0.0568\,x^2 + 0.00264\,x\,y^2 - 0.017\,x\,y - 0.249\,x + 0.00294\,y^3 - 0.0431\,y^2 + 0.216\,y + 0.873$	0.9906
	$-0.00224\,x^5 - 0.00132\,x^4\,y + 0.0361\,x^4 - 0.00134\,x^3\,y^2 + 0.0238\,x^3\,y - 0.234\,x^3 + 0.00739\,x^2\,y^2 - 0.12\,x^2\,y + 0.747\,x^2 + 0.00396\,x\,y^3 - 0.0339\,x\,y^2 + 0.261\,x\,y - 1.27\,x - 0.00469\,y^4 + 0.0258\,y^3 - 0.0708\,y^2 + 0.0654\,y + 1.14$	0.9960

Here, $x = \kappa_P$, $y = \kappa_N$ and $S = f(x, y)$

Table 5 Equations of the uprightness condition surfaces (Fig. 3 yellow surface) for the 3 cases along with the coefficient of determination. Here, $x = \kappa_P$, $y = \kappa_N$ and $S = f(x, y)$

θ_0	Surface ($f(x, y)$)	R^2
31°	$0.0577\,x^3\,y - 0.0458\,x^3 + 0.0111\,x^2\,y^2 - 0.0785\,x^2\,y + 0.486\,x^2 - 0.00431\,x\,y^3 + 0.256\,x\,y - 1.78\,x - 0.0025\,y^4 + 0.00306\,y^3 - 0.0199\,y^2 - 0.163\,y + 2.48$	0.9945
	$-0.0048\,x^5 - 0.00324\,x^4\,y + 0.0825\,x^4 - 0.00286\,x^3\,y^2 + 0.0577\,x^3\,y - 0.576\,x^3 + 0.0111\,x^2\,y^2 - 0.264\,x^2\,y + 1.91\,x^2 - 0.00431\,x\,y^3 - 0.0102\,x\,y^2 + 0.461\,x\,y - 3.1\,x - 0.0025\,y^4 + 0.0204\,y^3 - 0.0656\,y^2 - 0.0723\,y + 2.19$	0.9957
37°	$0.0113\,x^3\,y - 0.0476\,x^3 - 0.0867\,x^2\,y + 0.528\,x^2 - 0.00503\,x\,y^2 + 0.307\,x\,y - 2.02\,x - 0.00257\,y^2 - 0.263\,y + 2.91$	0.9950
	$0.0113\,x^3\,y - 0.0567\,x^3 - 0.0905\,x^2\,y + 0.509\,x^2 + 0.00491\,x\,y^2 + 0.23\,x\,y - 1.55\,x + 0.00762\,y^3 - 0.0468\,y^2 - 0.0278\,y + 1.79$	0.9910
44°	$0.00748\,x^3\,y - 0.0478\,x^3 - 0.0834\,x^2\,y + 0.557\,x^2 - 0.00441\,x\,y^2 + 0.313\,x\,y - 2.23\,x - +0.00132\,y^3 - 0.00585\,y^2 - 0.296\,y + 3.37$	0.9950
	$0.0106\,x^3\,y - 0.0524\,x^3 - 0.0924\,x^2\,y + 0.509\,x^2 + 0.0021\,x\,y^2 + 0.264\,x\,y - 1.69\,x + 0.00367\,y^3 - 0.0276\,y^2 - 0.116\,y + 2.13$	0.9927

Acknowledgements Sunder Neelakantan and Prashant K. Purohit acknowledge partial support for this work through an NSF Grant NSF CMMI 1662101. Saba Pasha acknowledges partial support for this work through a research grant from the Scoliosis Research Society and the National Institute of Health (NIH) R21 AR075971 01A1.

Compliance with ethical standards

Conflict of interest The authors declare that they have no conflict of interest.

Appendix

We present the sagittal view of the deformed configuration of the rods presented in Fig. 8 in Fig. 11. We see that the rods bend toward the **+ve y-** axis, which would be the case given a **-ve** $m_x(s)$ moment acting along the length of the rod.

We present the equations of the surfaces and the coefficient of determination($\boldsymbol{R^2}$) used in Fig. 3 in Tables 4 and 5. We present the equations of the loop–Lemniscate classification surfaces in Table 4. We also present the equations of the surfaces generated from the uprightness check in Table 5.

References

Antman S (2006) Nonlinear problems of elasticity. Applied Mathematical Sciences. Springer, New York

Audoly B, Pomeau Y (2010) From hair curls to the non-linear response of shells. Elasticity and geometry. OUP Oxford, Oxford

Belytschko T, Andriacchi T, Schultz A, Galante J (1973) Analog studies of forces in the human spine: computational techniques. J Biomech 6(4):361–371

Brink RC, Schlösser TP, van Stralen M, Vincken KL, Kruyt MC, Hui SC, Viergever MA, Chu WC, Cheng JC, Castelein RM (2018) Anterior–posterior length discrepancy of the spinal column in adolescent idiopathic scoliosis—a 3d ct study. Spine J 18(12):2259–2265

Burwell RG (2003) Aetiology of idiopathic scoliosis: current concepts. Pediatr Rehab 6(3–4):137–170

Castelein RM, Veraart B (1992) Idiopathic scoliosis: prognostic value of the profile. Eur Spine J 1(3):167–169

Castelein RM, van Dieen JH, Smit TH (2005) The role of dorsal shear forces in the pathogenesis of adolescent idiopathic scoliosis—a hypothesis. Med Hypotheses 65(3):501–508

Cheng JC, Castelein RM, Chu WC, Danielsson AJ, Dobbs MB, Grivas TB, Gurnett CA, Luk KD, Moreau A, Newton PO, Stokes IA, Weinstein SL, Burwell RG (2015) Adolescent idiopathic scoliosis. Nat Rev Disease Primers 1(1):15030

Chu WC, Lam WM, Ng BK, Tze-ping L, Lee K-M, Guo X, Cheng JC, Burwell RG, Dangerfield PH, Jaspan T (2008) Relative shortening and functional tethering of spinal cord in adolescent scoliosis—result of asynchronous neuro-osseous growth, summary of an electronic focus group debate of the IBSE. Scoliosis 3(1):8

Crisco JJ, Panjabi MM (1992) Euler stability of the human ligamentous lumbar spine. Part I: theory. Clin Biomech (Bristol, Avon) 7(1):19–26

Crisco JJ, Panjabi MM, Yamamoto I, Oxland TR (1992) Euler stability of the human ligamentous lumbar spine. Part II: experiment. Clin Biomech (Bristol, Avon) 7(1):27–32

de Reuver S, Brink R, Homans J, Kruyt M, van Stralen M, Schlösser T, Castelein R (2018) The changing position of the center of mass of the thorax during growth in relation to pre-existent vertebral rotation. SPINE 44(10):679–684

Duong L, Cheriet F, Labelle H (2006) Three-dimensional classification of spinal deformities using fuzzy clustering. Spine 31(8):923–30

Goto M, Kawakami N, Azegami H, Matsuyama Y, Takeuchi K, Sasaoka R (2003) Buckling and bone modeling as factors in the development of idiopathic scoliosis. Spine (Phila Pa 1976) 28(4):364–371

Gu S-X, Wang C-F, Zhao Y-C, Zhu X-D, Li M (2009) Abnormal ossification as a cause the progression of adolescent idiopathic scoliosis. Med Hypotheses 72(4):416–417

Janssen MMA, Kouwenhoven J-WM, Schlösser TPC, Viergever MA, Bartels LW, Castelein RM, Vincken KL (2011) Analysis of preexistent vertebral rotation in the normal infantile, juvenile, and adolescent spine. Spine 36(7):E486–91

Kouwenhoven J-WM, Vincken KL, Bartels LW, Castelein RM (2006) Analysis of preexistent vertebral rotation in the normal spine. Spine 31(13):1467–72

Liu Z, Tam EMS, Sun G-Q, Lam T-P, Zhu Z-Z, Sun X, Lee K-M, Ng T-B, Qiu Y, Cheng JCY, Yeung H-Y (2012) Abnormal leptin bioavailability in adolescent idiopathic scoliosis: an important new finding. Spine 37(7):599–604

Lucas DB (1970) Mechanics of the spine. Bull Hosp Joint Diseases Orthop Inst 31(2):115–131

Lucas DB, Boris B (1961) Stability of the Ligamentous Spine. N.p.: Biomechanics Laboratory, U of California. Print

Meakin JR, Hukins DWL, Aspden RM (1996) Euler buckling as a model for the curvature and flexion of the human lumbar spine. Proc R Soc Lond Ser B Biol Sci 263(1375):1383–1387

Neelakantan S, Purohit PK, Pasha S (2020) A semi-analytic elastic rod model of pediatric spinal deformity. J Biomech Eng (under review)

Nizette M, Goriely A (1999) Towards a classification of Euler–Kirchhoff filaments. J Math Phys 40(6):2830–2866

Pasha S (2019a) 3D deformation patterns of S-shaped elastic rods as a pathogenesis model for spinal deformity in adolescent idiopathic scoliosis. Sci Rep 9(1):16485

Pasha S (2019b) 3D spinal and rib cage predictors of brace effectiveness in adolescent idiopathic scoliosis. BMC Musculoskelet Disord 20:384

Pasha S, Baldwin K (2019a) Surgical outcome differences between the 3D subtypes of right thoracic adolescent idiopathic scoliosis. Eur Spine J 28:3076–3084

Pasha S, Baldwin K (2019b) Preoperative sagittal spinal profile of adolescent idiopathic scoliosis lenke types and non-scoliotic adolescents: A systematic review and meta-analysis. Spine (Phila Pa 1976) 44(2):134–142

Pasha S, Aubin CE, Sangole AP, Labelle H, Parent S, Mac-Thiong JM (2014a) Three-dimensional spinopelvic relative alignment in adolescent idiopathic scoliosis. Spine (Phila Pa 1976) 39(7):564–70

Pasha S, Aubin C-E, Parent S, Labelle H, Mac-Thiong J-M (2014b) Biomechanical loading of the sacrum in adolescent idiopathic scoliosis. Clin Biomech 29(3):296–303

Pasha S, Hassanzadeh P, Ecker M, Ho V (2019a) A hierarchical classification of adolescent idiopathic scoliosis: identifying the distinguishing features in 3d spinal deformities. PLOS ONE 14(3):1–12

Pasha S, Sankar WN, Castelein RM (2019b) The link between the 3d spino-pelvic alignment and vertebral body morphology in adolescent idiopathic scoliosis. Spine Deform 7(1):53–59

Pasha S, Smith L, Sankar WN (2019c) Bone remodeling and disc morphology in the distal unfused spine after spinal fusion in adolescent idiopathic scoliosis. Spine Deform 7(5):746–753

Pasha S (2020) What causes different coronal curve patterns in idiopathic scoliosis? bioRxiv. https://doi.org/10.1101/2020.01.21.913707.

Schlösser TP, Shah SA, Reichard SJ, Rogers K, Vincken KL, Castelein RM (2014) Differences in early sagittal plane alignment between thoracic and lumbar adolescent idiopathic scoliosis. Spine J 14(2):282–290

Schlösser TPC, Vincken KL, Rogers K, Castelein RM, Shah SA (2015) Natural sagittal spino-pelvic alignment in boys and girls before, at and after the adolescent growth spurt. Eur Spine J 24:1158–1167

Stokes IA, Aronsson DD, Spence H, Iatridis JC (1998) Mechanical modulation of intervertebral disc thickness in growing rat tails. J Spinal Disord 11(3):261–265

Weinstein SL, Dolan LA, Cheng JC, Danielsson A, Morcuende JA (2008) Adolescent idiopathic scoliosis. The Lancet 371(9623):1527–1537